Journal of Materials Chemistry A

Accepted Manuscript

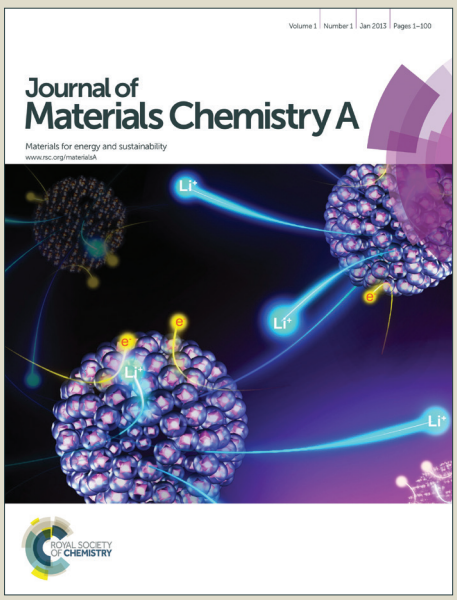

ROYAL SOCIETY OF CHEMISTRY

www.rsc.org/materialsA

Journal of Materials Chemistry A RSCPublishing

PAPER

A solvothermal strategy: One-step *in situ* synthesis of self-assembled 3D graphene-based composites with enhanced lithium storage capacity

Cite this: DOI: 10.1039/x0xx00000x

Received 00th January 2012,
Accepted 00th January 2012

DOI: 10.1039/x0xx00000x

www.rsc.org/

Jingjing Ma,[a] Jiuling Wang,[a] Yu-Shi He,*[a] Xiao-Zhen Liao,[a] Jun Chen,[b] Jia-Zhao Wang,[c] Tao Yuan,[a] Zi-Feng Ma[a]

A facile and controllable approach has been developed to synthesize three-dimensional (3D) graphene-based monoliths. Here, as a proof-of-concept experiment, self-assembled 3D CoO/graphene sheets (CoO/GS) composites with porous structures have been successfully fabricated in ethanol medium by a one-step, *in situ* growth, solvothermal method. During the process, the *in situ* nucleation and growth of CoO particles on GS were tuned by the formation of a 3D GS network. In the as-prepared composites, the self-assembled 3D GS network around the CoO particles can not only provide a 3D conductive matrix, but also buffer the volume changes of CoO and restrain the aggregation of CoO particles during charge/discharge cycling. The CoO particles, which are uniformly anchored into the 3D GS framework, can also act as spacers to effectively avoid the close restacking of GS. Compared to the bare CoO, the 3D CoO/GS composites as Li-ion battery anodes show dramatically improved electrochemical performance, including cycling stability and rate capability, owing to the unique self-assembled 3D structure and the superior synergistic effect between the two components. Such a synthesis strategy can be a promising route to produce diverse 3D graphene-based monoliths in various solvents.

Broader context

Graphene, a recently discovered carbonaceous material possessing a range of extraordinary properties, has attracted worldwide attention in the field of energy storage materials. The main problem in the preparation of the graphene-based composites presently is how to effectively reduce the agglomeration and restacking of graphene sheets in the preparation process to fully harness the unique properties of individual graphene sheet and adequately utilize the synergistic effect between graphene sheets (GS) and the other component. So there is an urgent need to develop novel three-dimensional (3D) graphene-based composites to retain the structure of the graphene network. In the current study, a simple, but effective and controllable solvothermal strategy has been developed to prepare 3D graphene-based monoliths. 3D self-assembled CoO/GS composites as anode materials for lithium ion batteries (LIBs) have been successfully fabricated in ethanol medium using a one-step, *in situ* growth, solvothermal method. As a consequence, the as-sythesized 3D CoO/GS composites show superior cycling and excellent rate performance even at a high current density. Most importantly, this study will be highly applicable for developing a range of 3D graphene-based monoliths in various solvents and thus will promote the research on the graphene-based energy storage materials.

Introduction

Possessing a combination of remarkable electrical, optical, thermal, and mechanical properties,[1, 2] graphene and graphene-based materials have shown outstanding potential for a variety of applications, including energy storage,[3-5] bio-applications,[6] flexible electronics,[7] sensors,[8] etc. In order to fully harness the unique properties of individual graphene sheet and adequately utilize the synergistic effect between GS and the other component, the main challenge in the synthesis of the graphene-based composites lies in how to effectively inhibit the restacking and agglomeration of GS. The conventional direct, high-temperature calcination can easily cause severe agglomeration of the GS.[9] More recently, many efforts have been made to retain the structure of the graphene network, such as keeping the graphene solvated by the vacuum filtration

method [10] and developing a range of 3D graphene-based composites by spray drying, *in situ* spray pyrolysis or hydrothermal technique.[11-15] The spray methods have been proved to be promising routes to massively produce for various 3D crumpled GS-wrapped composites.[11-13] Shi et al.[14] were the first to demonstrate that graphene hydrogels composed of a randomly cross-linked 3D GS network could be readily formed when a high concentration of graphene oxide (GO) dispersion is hydrothermally reduced without the addition of any reducing agent. Nevertheless, each particular material has to be prepared in a specific solvent. With the aid of the solvothermal reduction method, some researchers have found that GO dispersion can be directly reduced to GS dispersion in some solvents, such as N-methyl-2-pyrrolidinone (NMP),[16] ethanol,[17-19] ethylene glycol,[17] *N*,*N*-dimethylformamide (DMF),[20] and 1-butanol [17]. There are still few reports, however, on the direct preparation of self-assembled 3D graphene-based composites by the simple solvothermal reduction method. Recently, self-assembled 3D graphene-based organogels were prepared by solvothermal reduction of GO dispersion in propylene carbonate (PC).[21] Furthermore, using the solverthermal method and a following freeze-drying process, we have also successfully synthesized various 3D GS aerogels in different solvents, including NMP, ethanol, ethylene glycol and DMF (Fig. 1). The obtained 3D GS aerogels can maintain the porous structure of 3D GS organogels *via* a freeze-drying treatment, while a natural drying process will result in the drastic shrinkage of the 3D GS and impair the porous structure.

Transition metal oxides (MOs) have been regarded as promising anode materials for next-generation of rechargeable Li-ion batteries (LIBs) with high theoretical capacity (>600 mAh g^{-1}) compared to that of conventional graphite (372 mAh g^{-1}).[22] Unfortunately, the poor electrochemical performances of MOs, especially their cycling stability and rate capability, have hindered their practical application. This can be attributed to their low conductivity and drastic volume variation during the Li ion insertion/extraction processes, which cause electrode pulverization and loss of electrical continuity.[19] Flexible GS-wrapped MOs have been reported as an attractive option to alleviate the above problems.[23, 24] The obvious capacity degradation associated with the aggregation and pulverization of MO particles still exists, however, due to the loose contact between the GS and the MO particles.

Here, as a proof-of-concept experiment, we demonstrate a one-step, *in situ* growth, solvothermal method in ethanol medium to prepare 3D self-assembled CoO/GS composites. In order to effectively avoid the occurrence of a concentration gradient during the initial reaction stage, the CoO particles *in situ* grew on the surfaces of the GS and formed a more homogeneous composite, facilitating stronger interaction between the GS and the CoO particles with a tighter interface, which benefit the interfacial charge transfer and reduce the agglomeration and restacking of GS.[25] The solvothermal method offers significant advantages in preparation because no reducing agent, no filtration process, no calcination, and no protective atmosphere are required. When employed as anode for LIBs, CoO/GS delivers superior cycling performance with stable reversible capacity of about 434 mAh g^{-1} at the high current density of 6400 mA g^{-1}. Above all, such a facile solvothermal strategy can be adopted to develop a range of 3D graphene-based monoliths in different solvents.

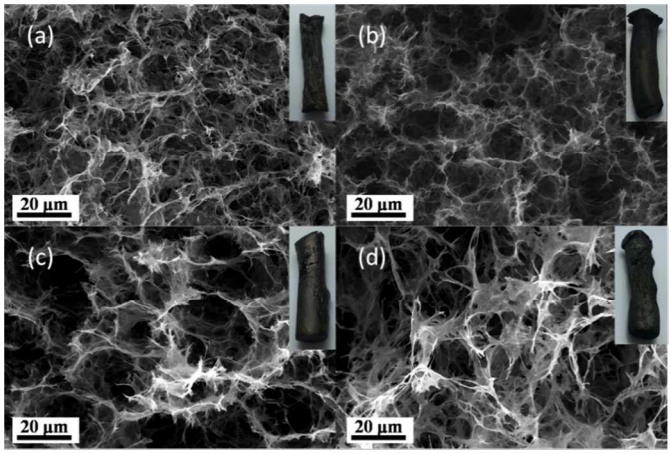

Fig. 1 SEM images of freeze-dried 3D GS aerogels obtained in different solvents (a) NMP, (b) ethanol, (c) ethylene glycol, and (d) DMF at 180 °C for 12 h in a Teflon-lined autoclave. Insets are the corresponding digital images. GO concentration: 1 mg mL^{-1}.

Experimental details

Synthesis of 3D CoO/GS.

Graphite oxide was synthesized from natural graphite powder (Grade 230, Asbury Carbons) by a modified Hummer's method.[26] The graphite oxide (5 mg) was exfoliated into 10 mL ethanol with the purity of 99.9% by sonication to form a GO suspension. Then, a certain amount of $Co(CH_3COO)_2{\cdot}4H_2O$ was added into the above solution in a weight ratio of $Co(CH_3COO)_2{\cdot}4H_2O$: GO of 15 : 1. The mixture was sealed in a glass sample vial. Thereafter, the vial was put into a Teflon-lined autoclave and maintained at 180 ^oC for 12 h. After cooling down to room temperature naturally, a black columniform product was obtained and then immersed in deionized water overnight to remove the residual ions, designated as CoO/GS (15). 3D CoO/GS (10) and CoO/GS (20) were synthesized by the same method, except that the weight ratios of the $Co(CH_3COO)_2{\cdot}4H_2O$: GO were 10 : 1 and 20 : 1, respectively. Pure CoO and GS samples were also prepared by the same procedure for comparison. All the as-prepared samples were freeze-dried for the following tests.

Structural and morphological characterization.

X-ray diffraction (XRD) measurements were carried out using a Rigaku D/MAX-2200/PC X-ray diffractometer at 40 kV and 20 mA, with a Cu Kα radiation source. Raman spectroscopy was used to identify the surface characteristics of the samples using a Bruker Optic SENTERRA (R-200L) with the laser wavelength of 633 nm at room temperature. Fourier transform infrared (FT-IR) measurements were carried out on a Perkin-Elmer 936 infrared spectrophotometer from KBr pellets in the

range of 500 — 4000 cm^{-1}. An X-ray photoelectron spectrometer (XPS, Kratos Axis Ultra DLD) was utilized to analyze the surface chemistries of the samples. Thermogravimetric analysis (TGA) was performed using a STA 449F3 analyzer (NETZSCH Co., Germany) to evaluate the residual level of CoO/GS composites. The morphology and microstructure of the samples were monitored using a FEI Nova SEM 230 ultra-high resolution Field emission scanning electron microscope (FESEM) equipped with energy dispersive X-ray spectroscopy (EDS, INCA X-Max 80, Oxford Instruments). Transmission election microscopy (TEM) and scanning TEM (STEM) were performed on an instrument (JEM-2100F, JEOL Ltd., Japan) equipped with EDS (INCA-IET200, Oxford Instruments) and operated at 200 kV.

Electrochemical measurements.

The CoO/GS composites were dried at 80 °C for 3h under Ar atmosphere. Then, 75 wt% active material (CoO/GS), 15 wt% acetylene black (Super-P), and 10 wt% polyvinylidene fluoride (PVDF) binder were mixed into N-methyl-2-pyrrolidinone (NMP). The obtained slurry was coated onto Cu foil disks to form the working electrode. The electrode was dried, cut into Φ14 mm sheets, pressed, and finally dried at 80 °C in vacuum for 4 h to remove the solvent. The amount of active materials loaded on the electrode was ~1.5 $mg \cdot cm^{-2}$.

CR2016 coin cells were assembled in an argon-filled glove box with lithium metal as the counter electrode and a UP3025 separator (provided by UBE Industries, Ltd., Japan). The electrolyte contained 1 M LiPF6 in dimethyl carbonate (DMC) and ethylene carbonate (EC) mixed solvent with a v/v ratio of 1:1 (LP30 from EM Industries, Inc.). Charge–discharge cycles of the half-cells were evaluated between 0.005 and 3 V vs. Li^+/Li at room temperature, using a LAND CT2001A model battery test system (Wuhan Jinnuo Electronics, Ltd.) under constant current conditions. The charge-discharge capacities were calculated based on the weight of CoO/GS materials in the electrode. Cyclic voltammetry (CV) measurements were carried out using a CHI instrument (CHI 660) at a scanning rate of 0.5 $mV\ s^{-1}$.

Results and Discussion

As shown in Fig. 2, the overall formation process of self-assembled 3D CoO/GS composite involves the following steps. Firstly, several drops of deionized water are added to GO and the water acted as a surfactant for wetting the surface of GO because it's difficult to disperse dried GO in pure ethanol. Next, $Co(CH_3COO)_2 \cdot 4H_2O$ is sonicated with the wetted GO in ethanol to form a uniform and opaque dispersion (Fig. 2a). The functional groups on the surfaces of the GO sheets with negative charge can then bind with Co^{2+} ions by electrostatic interactions and act as anchor sites. After that, the above mixture is solvothermally self-assembled at 180 °C for 12 h, thus forming a black ethanol gel of 3D CoO/GS (Fig. 2b). During the solvothermal reaction, OH^- ions, critical for the formation of CoO, could be produced by the esterification reaction between CH_3COO^- ions and ethanol.[27] Co^{2+} ions adsorbed on GO sheets react with OH^- ions to form CoO crystals under high temperature and pressure,[19, 27] while GO is simultaneously reduced and self-assembled to form the 3D GS network. The as-obtained 3D CoO/GS ethanol gel is washed and freeze-dried to maintain the 3D monolithic network to obtain the 3D CoO/GS aerogel (Fig. 2c). It is noteworthy that the shape of the 3D product depends on the geometry of the autoclave.

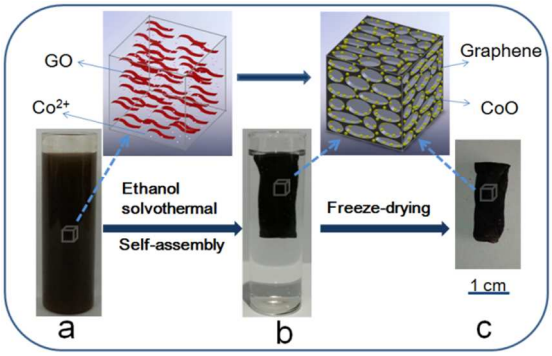

Fig. 2 Formation process of self-assembled 3D CoO/GS composite: a) uniform and opaque black dispersion of GO and $Co(CH_3COO)_2 \cdot 4H_2O$ in ethanol; b) 3D CoO/GS hybrid ethanol gel synthesized by solvothermal self-assembly in ethanol; c) 3D CoO/GS hybrid aerogel obtained after freeze-drying.

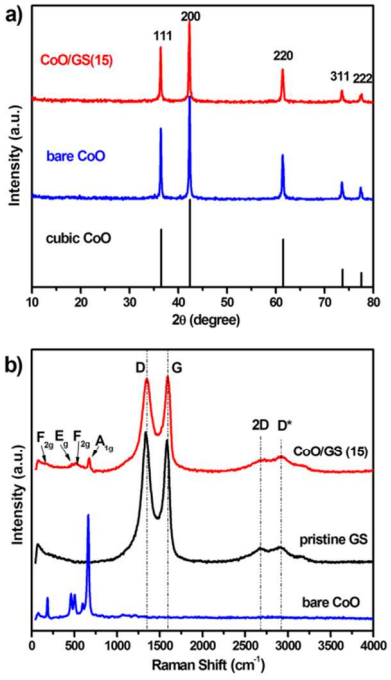

Fig. 3 (a) XRD patterns for the CoO/GS (15) and bare CoO. (b) Raman spectra for the CoO/GS (15), pristine GS, and bare CoO obtained using the standard procedure.

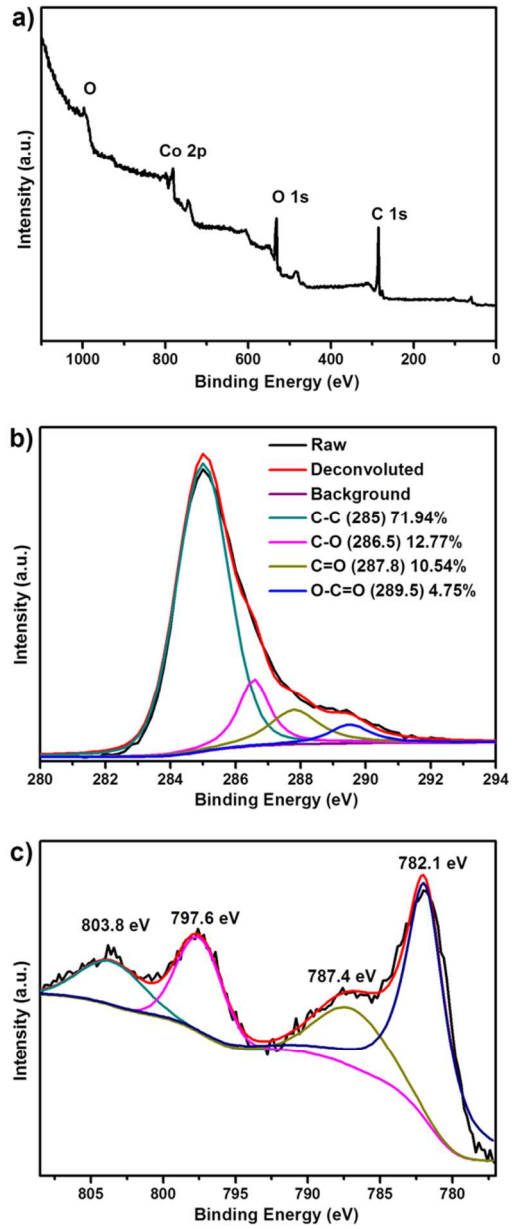

Fig 4. XPS spectra for the CoO/GS (15) composite: (a) survey spectrum and high-resolution (b) C 1s and (c) Co 2p spectra.

The XRD patterns of CoO/GS (15) and bare CoO are shown in Fig. 3a. For the CoO/GS (15) composite and the bare CoO, the major diffraction peaks at 2θ values of 36.5° (111), 42.4° (200), 61.5° (220), 73.7° (311), and 77.5° (222) match well with those of the standard cubic CoO (JCPDS 43-1004). No obvious characteristic peak of the GO at about 11° (Fig. S1†) is observed in the 3D CoO/GS (15) composite, which suggests that the GO was reduced to GS during the solvothermal process. Moreover, the characteristic (002) stacking peak of graphene at 22−28° (Fig. S1†) is also absent here, indicating that the graphene sheets are evenly dispersed without obvious stacking and were successfully covered with well-crystallized CoO. A similar phenomenon was also observed in the previous reports on graphene-based composites.[12, 28]

Fig. 3b presents the Raman spectra of CoO/GS (15), pristine GS, and bare CoO. In the CoO/GS (15), the peaks below 1000 cm^{-1} are consistent with the characteristic peaks of bare CoO. Characteristic peaks for carbon materials include the disordered D band at about 1350 cm^{-1}, the graphitic G band at about 1590 cm^{-1}, the 2D band at about 2700 $cm^{-1}$and D* at about 2900 cm^{-1}.[29] The distinct D band peak and the relatively small 2D peak indicate that numerous dangling bonds and defects, and much disordered structure are present.[30] These defects could act as nucleation sites for CoO particle growth and allow uniform formation of CoO particles in the 3D GS network.[31] Furthermore, in comparison with the pristine GS, shifting of the peaks can be clearly observed for both the D and G bands in the CoO/GS (15) composite, indicating significant charge transfer between the GS and the CoO particles. The charge transfer between GS and CoO can effectively improve the electrochemical performance of the CoO/GS composite.[32]

The FT-IR spectrum of the CoO/GS (15) composite shows peaks at 550 and 665 cm^{-1} that can be assigned to the vibrations of Co-O (Fig. S2†).[24] The peak located at 1224 cm^{-1} is derived from epoxy (C–O–C) groups, while the peak at 1570 cm^{-1} corresponds to the stretching vibration of C=C.[33]

XPS analysis was used to further characterize the surface chemical composition of CoO/GS (15) composite. The full XPS spectrum (Fig. 4a) indicates the presence of only the elements Co, O, and C in the composite. In Fig. 4b, four different peaks, which correspond to carbon sp^2 (C_g, ~285 eV), epoxy/hydroxyl groups (C–O, ~286.5 eV), carbonyl groups (C=O, ~287.8 eV), and carboxyl groups (O–C=O, ~289.5 eV), respectively, are detected.[34] The fraction of carbon−carbon bonding is about 71.9%, which is similar to the previously reported result.[12] This can be attributed to the efficient removal of oxygen functional groups from the GO by the solvothermal reaction process and demonstrates the formation of graphene. The high-resolution Co 2p spectrum of the 3D composite is shown in Fig. 3c. The peaks at 782.1 and 797.6 eV with a 15.5 eV peak-to-peak separation correspond to the binding energy of Co 2p 3/2 and Co 2p 1/2 of CoO, respectively, while two weak peaks at 787.4 and 803.8 eV could be the shake-up satellite peaks above two main peaks, indicating the presence of Co (Ⅱ).[28] The aforementioned XRD, Raman, FT-IR, and XPS characterizations confirm the successful preparation of CoO/GS composite.

The FESEM images in Fig. 5 show the surface morphologies of (a, b) bare CoO (c, d) pristine GS, and (e, f) CoO/GS (15). The SEM images of the bare CoO (Fig. 5a and 5b) display irregular particles about 200-500 nm in diameter with rough surfaces. From Fig. 5c and 5d, it can be clearly observed that the pure GS forms an easily recognizable and interconnected 3D porous framework with the pore sizes ranging from submicrometer to several micrometres. The formation of the self-assembled 3D GS framework is derived from the regional overlapping and coalescing of flexible GS through π-π stacking interactions during solvothermal treatment.[14, 35] As shown in

Fig. 5e and 5f, CoO/GS (15) still possesses a fully interconnected macroporous architecture, which is similar to that of pristine GS, but it is evident that the pore sizes of the 3D GS network in the composite have become much larger due to the introduction of CoO particles. The sphere-like CoO particles with a mean diameter of about 350 nm in the CoO/GS (15) composite are uniformly and closely anchored into the 3D GS network, suggesting effective assembly between the CoO particles and the GS during solvothermal treatment. The surface morphology of the CoO particles in the composite is also totally different from that of the bare CoO, which is ascribed to the oxygen-containing functional groups (hydroxyl, carboxyl, epoxy, etc.) on GO surfaces/edges, which could improve the crystallization of CoO and also act as anchor sites for *in situ* formation of CoO particles.[36] It is notable that most of the CoO particles are clearly encapsulated in the GS matrix, and the graphene shells present a typical crumpled and rippled morphology (Fig. 5f). It has been reported that the crumpled GS encapsulation not only enhances interface contact, but also suppresses the aggregation of particles and provides elastic void spaces to accommodate the strain and stress of the volume changes in the electrode materials during cycling.[37]

EDS mappings over a relatively large area (about 4 μm × 4 μm) for the elements carbon, oxygen and cobalt elements (Fig. S3†) indicate that the CoO particles are uniformly distributed in the 3D GS network. The graphene layer on some CoO surfaces may be too thin to be visible in the SEM image. So combined with EDS analysis (Fig. 6f), a STEM image (Fig. 6a) and corresponding elemental mapping images (Fig. 6c-e) of the small region indicated in Fig. 6b provide additional evidence to further confirm the homogeneous distribution of carbon, oxygen and cobalt on the surface of each individual CoO particle.

Microstructures of various samples were further characterized by TEM and high-resolution TEM (HRTEM) (Fig. 7). A typical TEM image of the as-prepared bare CoO sample can be observed in Fig. 7a. The morphology of the CoO particles, which have rough surfaces, is irregular, which is identical with the SEM observation. The corresponding selected-area electron diffraction (SAED) pattern (inset in Fig. 7a) shows clear diffraction spots, demonstrating the single-crystal-like nature of the CoO. In Fig. S4†, the pure GS exhibits a transparent feature with a wrinkled structure. Fig. 7b and 7c display TEM images of the CoO/GS (15) composite. As expected, the CoO particles are well wrapped by the GS and are distributed homogeneously in the network. The inset in Fig. 7b presents the corresponding SAED pattern of the CoO/GS (15) hybrid. There are two sets of diffraction patterns that belong to the CoO and the GS, respectively. Note that the weak diffraction rings from GS are obvious due to the multilayer graphene, while the diffraction spots for CoO demonstrate the single-crystalline nature of the CoO in the CoO/GS (15) composite.[24, 27] The HRTEM image of the CoO/GS (15) composite in Fig. 7d indicates that the CoO particle is encapsulated by multiple overlapping GS sheets. The regular lattice fringes also show a spacing of 0.24 nm, which can be assigned to the (111) plane of CoO.[24] In addition, the

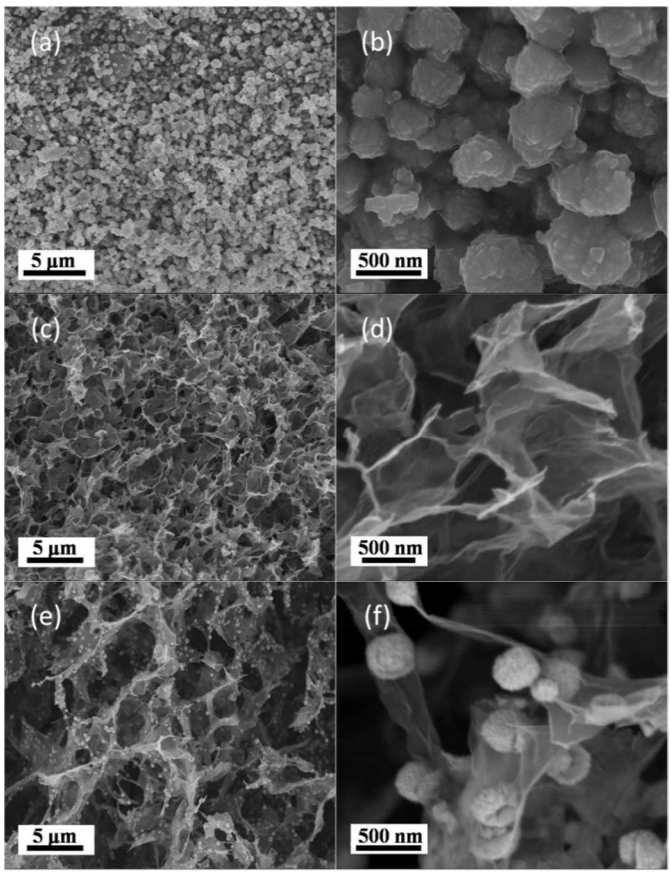

Fig. 5 FESEM images of (a, b) bare CoO, (c, d) pristine GS, and (e, f) CoO/GS (15).

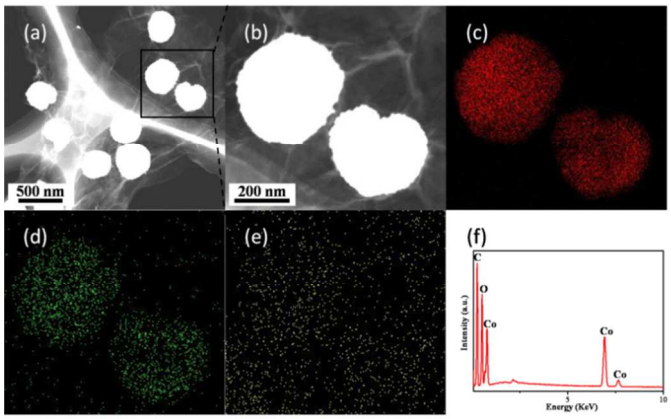

Fig. 6 STEM, elemental mapping, and EDS spectrum of CoO/GS (15): (a) typical STEM image; (b) STEM image taken from the square region marked in (a) and corresponding elemental mapping images of (c) Co, (d) O, and (e) C; and (f) EDS spectrum. These results suggest the homogeneous distribution of Co, O, and C in CoO/GS (15).

graphene content in the CoO/GS composite could significantly influence the morphology of the product. Based on the TEM images of CoO/GS (10) (Fig. S5a†), CoO/GS (15) (Fig. 7b) and CoO/GS (20) (Fig. S5b†), it can be found that with decreasing of graphene content, the sizes of the CoO particles gradually become larger. This result demonstrates that the size of the as-

synthesized material particles in the 3D GS network is controllable by the *in situ* growth in the solvothermal process.

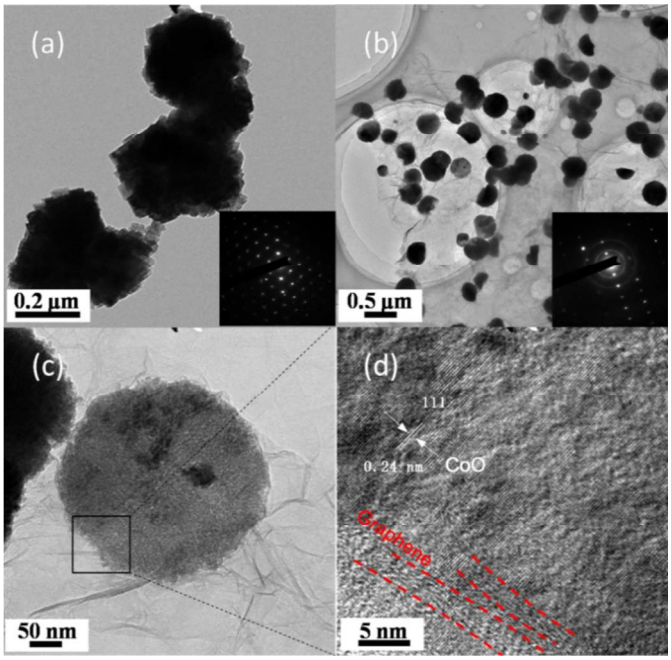

Fig. 7 TEM images of (a) bare CoO and (b-c) CoO/GS (15); (d) HRTEM image of CoO/GS (15). The insets in (a) and (b) are the electronic diffraction patterns of bare CoO and CoO/GS (15), respectively.

For quantifying the amount of graphene in the CoO/GS composites, TGA was carried out at a heating rate of 10 °C min^{-1} from 40 °C to 750 °C in air. In Fig. S6†, the weight change between about 220 and 600 °C could be due to the combustion of the graphene and the oxidation of CoO.[24, 38] According to the XRD analysis (Fig. S7†), the calcination product of CoO/GS (15) at 600 °C was Co_3O_4. Therefore, the weight fractions of graphene in the CoO/GS (10), CoO/GS (15), and CoO/GS (20) were calculated to be ~22.6%, 16.3%, and 11.5%, respectively.

Fig. 8 shows the electrochemical performance of the CoO/GS (15) composite. To identify the mechanism of the electrochemical reactions, the CV profiles of the CoO/GS (15) for the first, second, and tenth cycles were measured at a scan rate of 0.5 mV s^{-1}, as shown in Fig. 8a. In the cathodic polarization process of the first cycle for CoO/GS (15), two peaks, one obvious and one inconspicuous, were observed at about 0.28 and 0.98 V, which were ascribed to the Li insertion into CoO/GS composite and the formation of a solid electrolyte interphase (SEI) film.[38] Apparently, the reaction is related to the occurrence of some irreversible processes in the first cycle. Meanwhile, one broadened peak was recorded at about 2.2 V in the anodic process, corresponding to the reversible oxidation of cobalt to cobalt oxide.[39] During the subsequent cycles, the cathodic shifts to higher voltage potentials and the CV curves show good reproducibility, suggesting good reversible reactions. For the CoO/GS electrode, the electrochemical reversible reaction mechanism of Li with CoO and carbon in the lithium ion battery could be described as follows:[40]

$$CoO + 2Li^+ + 2e^- \Leftrightarrow 2Co + Li_2O \quad (1)$$

$$6C + Li^+ + e^- \Leftrightarrow LiC_6 \quad (2)$$

Fig. 8b shows the charge (delithiation) and discharge (lithiation) voltage profiles for the CoO/GS (15) composite at a current density of 200 mA g^{-1} at room temperature. In the first discharge cycle, an extended potential plateau at around 0.8 V demonstrates the conversion reaction and the formation of SEI film, which is consistent with the CV results. The reversible capacity (about 1000 mAh g^{-1}) of the composite are much higher than the theoretical capacity of CoO (716 mAh g^{-1}), which may be derived from the decomposition of electrolyte, the formation of the SEI layer, extra lithium-ion adsorption/desorption on the SEI layer, and the reduction of oxygenated functional groups on the surface of the graphene in the CoO/GS (15) composite.[41-46] Furthermore, it was reported that graphene can also contribute additional lithium storage capacity apart from the intrinsic theoretical capacity, which is due to significant disorder/defects in the graphene.[38,47] The coulombic efficiency (CE) of the CoO/GS (15) composite is around 77% at the first cycle and CE rises to more than 98% after 1 cycle. For the composite, it is notable that no obvious capacity loss was observed after 2 cycles, and the electrode could still maintain a reversible capacity of approximately 960 mAh g^{-1} after 10 cycles.

To evaluate the electrode kinetics of bare CoO, CoO/GS (10), CoO/GS (15), and CoO/GS (20), the rate capability of the samples is shown in Fig. 8c. It is clearly seen that the CoO/GS composites, especially the CoO/GS (15) composite with 16.3% graphene, have much better rate performance compared to the reference bare CoO and other CoO/GS composites. When the charge/discharge current density increases to 1600 mA g^{-1}, the reversible capacity of the CoO/GS (15) composite still keeps to a stable value above 730 mAh g^{-1}. In contrast, at this high rate, the bare CoO can only deliver an average reversible capacity of ~ 270 mAh g^{-1}. When the current density is returned to 200 mA g^{-1}, the CoO/GS (15) electrode can still reveal a high reversible capacity (1036 mAh g^{-1}, 95.5% of the initial reversible capacity) after the 50th cycle, indicating good reversibility.

The discharge-charge cycling performance of CoO/GS (15) at high current densities was further evaluated in Fig. 8d. All cells were cycled at a current density of 200 mA g^{-1} for the initial two cycles before each test. The composite exhibited good cycling performance at high current densities. After 50 cycles, stable reversible capacities of about 706 and 503 mAh g^{-1} could still be retained at current densities of 1600 and 4800, respectively. Moreover, the high-rate cycling performance of the CoO/GS (15) composite is much better than that of the bare CoO, which has a reversible capacity of only 211 mAh g^{-1} after the same 50 cycles at a current density of 1600 mA g^{-1}. The metallic lithium counter electrode will play a very important role at higher current densities, hence we evaluated the cycling performance of CoO/GS (15) at a current density of 6400 mA g^{-1} using a three-electrode system (MTI Corporation, Fig. S8).

As shown in Fig. 9, the reversible capacity of about 434 mAh g^{-1} could still be retained after 50 cycles.

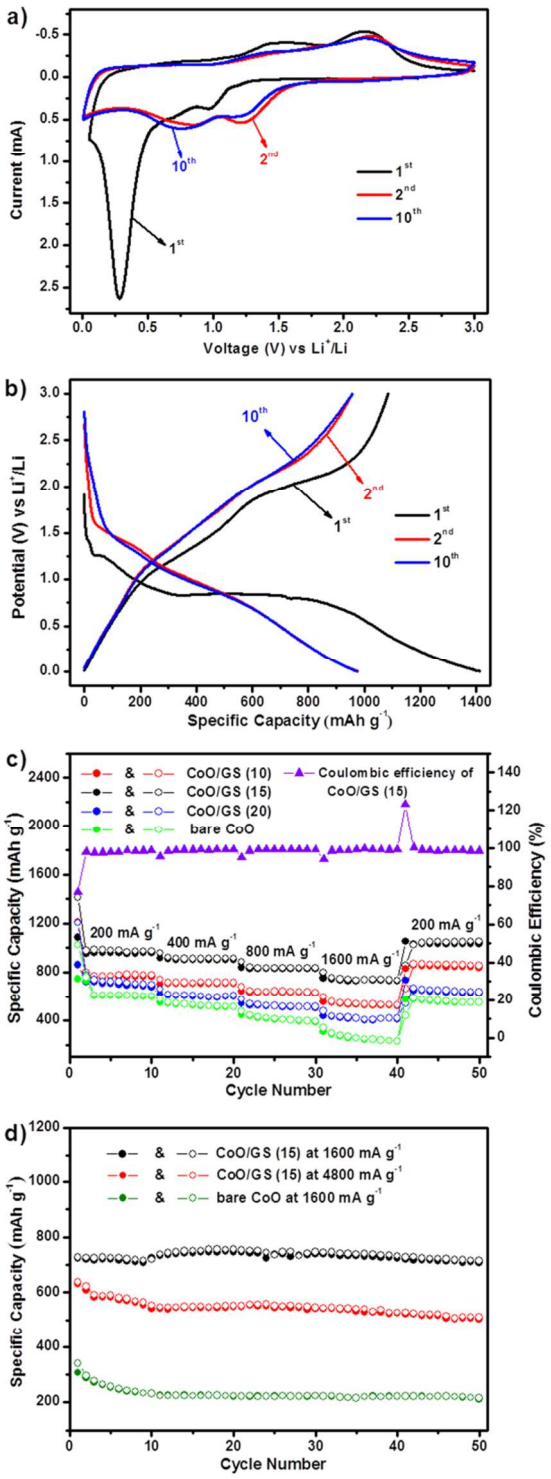

Fig. 8 (a) CV curves of the CoO/GS (15) composite in the potential range of 0.005–3 V at a scan rate of 0.5 mV s^{-1}. (b) Charge–discharge curves of the CoO/GS (15) composite at a current density of 200 mA g^{-1}. (c) Rate performance of the CoO/GS composites with different graphene contents and bare CoO at various current densities. (d) Cycling behavior of bare CoO and CoO/GS (15) at high current densities. Hollow and solid point symbols represent lithium insertion and extraction, respectively.

Evidently, the CoO/GS composites show significantly enhanced cycling and rate performance, perhaps because they have benefited from the unique self-assembled 3D structure of GS and the simultaneous growth of CoO particles anchored into the 3D GS framework during the solvothermal route, which can ensure the integrity of the electrodes over many discharge/charge cycles. This could be confirmed by examining variation in the microstructure of the bare CoO and the CoO/GS (15) composite after 50 cycles at a charge/discharge current density of 1600 mAh g^{-1} using TEM (Fig. S9†). In Fig. S9a†, it is clearly observed that the bare CoO particles have become smaller and cracked after 50 cycles, indicating that it is the pulverization of the particles during cycling that leads to the poor cycling stability of bare CoO particles. In contrast, in Fig. S9b†, the CoO particle anchored into GS still retained its original morphology and did not further break after 50 cycles. This demonstrates the long-term stability of the as-obtained CoO/GS (15) during cycling, and the pulverization of the CoO particles is inhibited under the protection of the flexible 3D GS network.

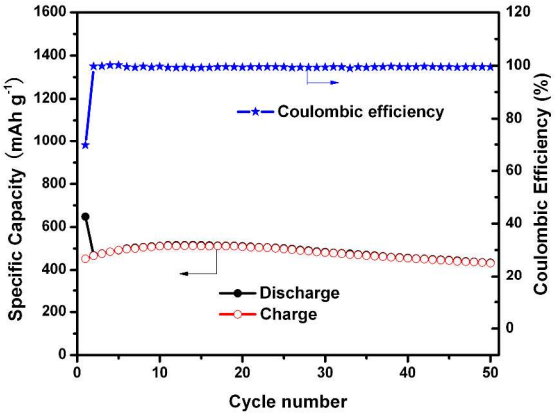

Fig. 9 Cycling performance of CoO/GS (15) in a three-electrode system at a current density of 6400 mA g^{-1}.

Overall, the improved cycling and rate performance of the CoO/GS composites as anode materials for lithium storage may be attributed to the following three aspects: First, almost every individual CoO particle can be encapsulated in GS and maintain intimate contact with GS *via* the one-step, *in situ* growth, solvothermal process. Second, the self-assembled GS in the CoO/GS composites constitutes not only a 3D continuous and highly conductive network, but also provides elastic void spaces to buffer the strain and stress of the volume changes of CoO and inhibit the aggregation and pulverization of CoO particles during cycling, thus ensuring favorable transport kinetics for lithium ions and electrons. Third, CoO particles are uniformly anchored into the GS matrix as spacers, which can effectively prevent the close restacking of GS and consequently maintain the large contact area between the electrode and electrolyte.

Conclusions

In conclusion, a simple, but effective and controllable method has been developed to prepare 3D graphene-based monoliths. Here, 3D self-assembled CoO/GS aerogels, which can be used as anode materials for LIBs, have been successfully fabricated in ethanol medium by a one-step, *in situ* growth, solvothermal method and a subsequent freeze-drying process. In this way, CoO particles can nucleate *in situ* and grow on the surface of the GS with the simultaneous formation of the 3D GS network. In such a unique macroporous structure, CoO particles are evenly anchored into the GS matrix. The 3D GS in the composites not only acts as an electronically conductive matrix, but also provides double protection against the aggregation and pulverization of CoO particles during cycling, so that the synergistic effect between the 3D GS and the active particles is fully utilized. As a consequence, the as-formed 3D CoO/GS composites show superior cycling stability and rate capability. The different forms of graphene-based materials can be used in various applications because the outcome is likely to vary with size, morphology and chemical structure. So our study suggests that the size of as-synthesized material particles in the 3D GS architecture can be further controlled for other applications by changing the concentration of reactants, reaction temperature and reaction time. Most importantly, this study also forms the basis for developing various 3D graphene-based monoliths in different solvents by the one-step solvothermal strategy for wide applications in the near future.

Acknowledgements

We are grateful for financial support for this work from the National Basic Research Program of China (2014CB239700), the Natural Science Foundation of China (21336003, 21006063, 21073120, 51272156), and China Postdoctoral Science Foundation (2013M541510).

Notes and references

[a] Institute of Electrochemical and Energy Technology, Department of Chemical Engineering, Shanghai Jiao Tong University, Shanghai, 200240, China; Tel: +86-21-54744533; Fax: +86-21-54747717; E-mail: ys-he@sjtu.edu.cn
[b] Intelligent Polymer Research Institute, ARC Centre of Excellence for Electromaterials Science, University of Wollongong, Wollongong, NSW, 2522, Australia.
[c] Institute for Superconducting and Electronic Materials, University of Wollongong, Wollongong, NSW, 2522, Australia.

† Electronic Supplementary Information (ESI) available: additional XRD, FT-IR, EDS mapping, TEM images, TGA. See DOI: 10.1039/b000000x/

1 K. S. Novoselov, A. K. Geim, S. V. Morozov, D. Jiang, Y. Zhang, S. V. Dubonos, I. V. Grigorieva and A. A. Firsov, *Science*, 2004, **306**, 666-669.
2 C. N. Rao, A. K. Sood, K. S. Subrahmanyam and A. Govindaraj, *Angew. Chem. Int. Ed.*, 2009, **48**, 7752-7777.
3 H. Jiang, P. S. Lee and C. Li, *Energy & Environ. Sci.*, 2013, **6**, 41-53.
4 S. Ivanovici and K. Müllen, *Angew. Chem. Int. Ed.*, 2010, **49**, 8408-8411.
5 Y.-S. He, D.-W. Bai, X. Yang, J. Chen, X.-Z. Liao and Z.-F. Ma, *Electrochem. Commun.*, 2010, **12**, 570-573.
6 J. Lu, Y.-S. He, C. Cheng, Y. Wang, L. Qiu, D. Li and D. Zou, *Adv. Funct. Mater.,* 2013, **23**, 3494-3502.
7 T.-H. Han, Y. Lee, M.-R. Choi, S.-H. Woo, S.-H. Bae, B. H. Hong, J.-H. Ahn and T.-W. Lee, *Nature Photonics*, 2012, **6**, 105-110.
8 W. Yang, K. R. Ratinac, S. P. Ringer, P. Thordarson, J. J. Gooding and F. Braet, *Angew. Chem. Int. Ed.*, 2010, **49**, 2114-2138.
9 Y. Wang, Z. Shi, Y. Huang, Y. Ma, C. Wang, M. Chen and Y. Chen, *J. Phys. Chem. C*, 2009, **113**, 13103-13107.
10 X. Yang, J. Zhu, L. Qiu and D. Li, *Adv. Mater.*, 2011, **23**, 2833-2838.
11 Y.-S. He, P. Gao, J. Chen, X. Yang, X.-Z. Liao, J. Yang and Z.-F. Ma, *RSC Adv.*, 2011, **1**, 958-960.
12 G.-W. Zhou, J. Wang, P. Gao, X. Yang, Y.-S. He, X.-Z. Liao, J. Yang and Z.-F. Ma, *Ind. Eng. Chem. Res.*, 2013, **52**, 1197-1204.
13 A. Chidembo, S. H. Aboutalebi, K. Konstantinov, M. Salari, B. Winton, S. A. Yamini, I. P. Nevirkovets and H. K. Liu, *Energy Environ. Sci*., 2012, **5**, 5236-5240.
14 Y. Xu, K. Sheng, C. Li and G. Shi, *ACS Nano*, 2010, **4**, 4324-4330.
15 Z. S. Wu, Y. Sun, Y. Z. Tan, S. Yang, X. Feng and K. Müllen, *J. Am. Chem. Soc.*, 2012, **134**, 19532-19535.
16 S. Dubin, S. Gilje, K. Wang, V. C. Tung, K. Cha, A. S. Hall, J. Farrar, R. Varshneya, Y. Yang and R. B. Kaner, *ACS Nano*, 2010, **4**, 3845-3852.
17 C. Nethravathi and M. Rajamathi, *Carbon*, 2008, **46**, 1994-1998.
18 S. P. Lim, N. M. Huang and H. N. Lim, *Ceram. Int.*, 2013, **39**, 6647-6655.
19 J. Zhu, T. Zhu, X. Zhou, Y. Zhang, X. W. Lou, X. Chen, H. Zhang, H. H. Hng and Q. Yan, *Nanoscale*, 2011, **3**, 1084-1089.
20 F. He, N. Niu, F. Qu, S. Wei, Y. Chen, S. Gai, P. Gao, Y. Wang and P. Yang, *Nanoscale*, 2013, **5**, 8507-8516.
21 Q. Zhou, J. Gao, C. Li, J. Chen and G. Shi, *J. Mater. Chem. A*, 2013, **1**, 9196-9201.
22 P. Poizot, S. Laruelle, S. Grugeon, L. Dupont and J. -M. Tarascon, *Nature*, 2000, **407**, 496-499.
23 M. Zhang, M. Jia, Y. Jin and X. Shi, *Appl. Surf. Sci.*, 2012, **263**, 573-578.
24 Y. Qi, H. Zhang, N. Du and D. Yang, *J. Mater. Chem., A*, 2013, **1**, 2337-2342.
25 J. Zhou, G. Tian, Y. Chen, X. Meng, Y. Shi, X. Cao, K. Pan and H. Fu, *Chem. Commun.*, 2013, **49**, 2237-2239.
26 D. Li, M. B. Müller, S. Gilje, R. B. Kaner and G. G. Wallace, *Nature Nanotech.*, 2008, **3**, 101-105.
27 Y. Ye, F. Yuan and S. Li, *Mater. Lett.*, 2006, **60**, 3175-3178.
28 Y. Sun, X. Hu, W. Luo and Y. Huang, *The J. Phys. Chem. C*, 2012, **116**, 20794-20799.
29 A. C. Ferrari, J. C. Meyer, V. Scardaci, C. Casiraghi, M. Lazzeri, F. Mauri, S. Piscanec, D. Jiang, K. S. Novoselov, S. Roth and A. K. Geim, *Phys. Rev. Lett.*, 2006, **97**, 187401.
30 L. Yin, J. Wang, F. Lin, J. Yang and Y. Nuli, *Energy Environ. Sci.*, 2012, **5**, 6966-6972.
31 K. Evanoff, A. Magasinski, J. Yang and G. Yushin, *Adv. Energy Mater.*, 2011, **1**, 495-498.

32 W. Chen, S. Li, C. Chen and L. Yan, *Adv. Mater.*, 2011, **23**, 5679-5683.
33 J. Zhou, H. Song, L. Ma and X. Chen, *RSC Adv.*, 2011, **1**, 782-791.
34 H. Tang, G. J. Ehlert, Y. Lin and H. A. Sodano, *Nano lett.*, 2012, **12**, 84-90.
35 Y. Sun, Q. Wu and G. Shi, *Phys. Chem. Chem. Phys.,* 2011, **13**, 17249-17254.
36 J. Yuan, J. Zhu, H. Bi, X. Meng, S. Liang, L. Zhang and X. Wang, *Phys. Chem. Chem. Phys.*, 2013, **15**, 12940-12945.
37 Z. S. Wu, S. Yang, Y. Sun, K. Parvez, X. Feng and K. Müllen, *J. Am. Chem. Soc.*, 2012, **134**, 9082-9085.
38 C. Peng, B. Chen, Y. Qin, S. Yang, C. Li, Y. Zuo, S. Liu and J. Yang, *ACS Nano*, 2012, **6**, 1074-1081.
39 F. D. Wu and Y. Wang, *J. Mater. Chem.*, 2011, **21**, 6636-6641.
40 X. Huang, R. Wang, D. Xu, Z. Wang, H. Wang, J. Xu, Z. Wu, Q. Liu, Y. Zhang and X. Zhang, *Adv. Funct. Mater.*, 2013, 23, 4345-4353.
41 L. Su, Z. Zhou and P. Shen, *Electrochimi. Acta,* 2013, **87**, 180-185.
42 L. Su, Y. Jing and Z. Zhou, *Nanoscale*, 2011, **3**, 3967-3983.
43 L. Su, Z. Zhou and P. Shen, *J. Phys. Chem. C*, 2012, **116**, 23974−23980.
44 S. Laruelle, S. Grugeon, P. Poizot, M. Dollé, L. Dupont, and J. -M. Tarascon, *J. Electrochem. Soc*., 2002, **149**, A627-A634.
45 L. Su, Y. Zhong and Z. Zhou, *J. Mater. Chem.,* A, 2013, **1**, 15158-15166.
46 L. Su, Z. Zhou, X. Qin, Q. Tang, D. Wu, P. Shen, *Nano Energy*, 2013, **2**, 276-282.
47 D. Pan, S. Wang, B. Zhao, M. Wu, H. Zhang, Y. Wang and Z. Jiao, *Chem. Mater.*, 2009, **21**, 3136-3142.